Check for updates

Tuning diffusion coefficient, ionic conductivity, and transference number in rGO/BaCoO₃ electrode material for optimized supercapacitor energy storage†

Mohsin Shahzad,[a] Farooq Ahmad, ID *[ab] M. Ibraheem,[a] Abdul Shakoor,[a] Shahid M. Ramay,[c] M. Rafi Raza[d] and Shahid Atiq ID *[a]

Due to their remarkable cycle stability and outstanding capacitance, ABO₃-type perovskite materials have emerged as highly effective electrode materials, delivering remarkable electrochemical performance. In this study, BaCoO₃/rGO composites with varying rGO content (0, 5, 10, and 15%), designated as PBCO, BCO-I, BCO-II, and BCO-III, were synthesized using a solvothermal process. These composites were evaluated for their potential as electrode materials in supercapacitor (SC) applications. X-ray diffraction analysis confirmed the presence of well-crystallized samples with a hexagonal phase structure. Field emission scanning electron microscopy revealed the desired level of porosity, well-defined morphologies, and uniformly distributed grains, which are beneficial for electrochemical applications. Elemental analysis verified the stoichiometric composition of the samples. Comprehensive electrochemical characterization was performed using cyclic voltammetry in a 2 M KOH solution, revealing a transition from diffusive control (EDLC) to hybrid capacitor behavior. Additionally, galvanostatic charge–discharge experiments demonstrated that the BCO-III composite exhibited a specific capacity of 90.15 C g^{-1}, an energy density of 21.28 W h kg^{-1}, and a power density of 531.25 W kg^{-1}. The transference number (t_+) is found to be 0.2, which means that higher current will be driven through the anion. Further, the sample BCO-III, exhibiting the highest specific capacity, was evaluated for stability and demonstrated a remarkable retention rate of 90% after 5k GCD cycles and a remarkable coulombic efficiency of 94%, with an excellent diffusion rate and ionic conductivity of about 4.51 × 10^{-14} cm^2 s^{-1}, 0.128 S cm^{-1}, respectively, highlighting its significant potential for SC applications.

1. Introduction

Extensive usage of fossil fuels results in excessive greenhouse gas emissions such as methane (CH_4) and carbon dioxide (CO_2), escalating the threat of world conflict and climate change and its effects on the planet. Therefore, it is essential to advance renewable energy technologies and decarbonize fuel. The sporadic nature of these sources, like solar and wind, continues to be the primary obstacle to increasing the efficiency of renewable energy systems (RESs).[1] The only way to solve these

challenges is to build a community free of carbon and dependent on clean and renewable energy resources. To meet energy and environmental requirements, the world has been forced to reevaluate its power strategy.[2] This rising need has made developing energy storage systems (ESS) with more extensive and better capacities possible. From this perspective, energy from numerous irregular renewable sources, such as wind, waves, and sun, might be considered beneficial sources.[3] Therefore, the energy produced from these sources must be stored to be made available wherever required.[4] For this purpose, effective energy storage technologies, including batteries and electrochemical SCs, have been explored.[5] Over the last two decades, SCs have steadily replaced batteries thanks to their remarkable operating voltage and specific capacitance (C_{sp}).[6–10]

SCs are supposed to be one of the emerging energy storage devices (ESDs) due to their tremendous power density (PD) (10^5 W kg^{-1}), long cyclic stability (>10^6 charge–discharge cycle), and low maintenance requirements.[11] Unfortunately, because of their energy density (ED), SCs can only be used in systems that

[a]*Centre of Excellence in Solid State Physics, University of the Punjab, Lahore 54590, Pakistan. E-mail: satiq.cssp@pu.edu.pk*

[b]*Institute of Molecular Physics Polish Academy of Sciences Poznan, Poznan, Poland. E-mail: farooq.ahmad@ifmpan.poznan.pl*

[c]*Department of Physics and Astronomy, King Saud University (KSU), Riyadh, Saudi Arabia*

[d]*Department of Mechanical Engineering, COMSATS University Islamabad, Sahiwal Campus, Sahiwal, Pakistan*

† Electronic supplementary information (ESI) available. See DOI: https://doi.org/10.1039/d4ra08894h

require a quick power supply, such as bullet trains and backup power sources.[12] There are two categories of SCs based on the energy storage mode. These categories are electric double-layer capacitors (EDLCs) and pseudo-capacitors (PCs).[13] The EDLCs store charges through the adsorption/desorption of ions into porous materials (commonly carbon-based).[14] They possess exceptional PD but low ED.[15] On the other hand, in PCs, the energy storage is governed by fast reversible redox reactions.[16] The electrode material for such capacitors is composed of transition metal oxide (TMOs), conducting polymers (CPs), and metal hydroxides.[17] These electrode materials exhibit excellent capacitance but poor ED.[18]

The features of electrode materials will significantly impact the electrochemical behavior of SCs.[18] The selected electrode should have strong conductivity and an elevated specific surface area (SSA) to achieve an excellent specific capacity.[19] A few years ago, pseudocapacitive materials attracted considerable interest because their energy storage was more than that of EDLCs.[20] However, ABO_3-type perovskite materials, compared to TMOs and TMDs, are captivating candidates as electrode materials for SCs. Due to their extraordinary electrochemical performance, ABO_3-type perovskite materials, such as $BaCoO_3$, $SrCoO_3$, and $MnFeO_3$ have been widely used as electrode materials for SCs for a long time. Such 2D materials have restricted commercial production because of their toxicity and prohibitive costs. In addition to perovskite materials, it is essential to note that cobalt oxide (Co_3O_4) is inexpensive and easy to make.[21–24] Unfortunately, the perovskite materials suffer from low-rate capacitance and limited reversibility; some are uncommon and expensive. Contrarily, carbon-based materials like carbon nanotubes (CNTs) have gained interest as electrode materials for SCs because of their significant electrical conductivity and chemical stability.[25]

Graphene consists of a continuous thin sheet of carbon with sp^2 bonds. Geim and Novoselov identified graphene in 2004 via the 'scotch tape' approach, and as a result, graphene is now widely used in many industries. Similarly, derivatives of graphene or functionalized graphene, such as GO and rGO, are assembled using different reduction techniques and are equally favorable.[26] Compared to many other carbon compounds, GO, with its exceptional electrical conductivity, mechanical flexibility, and SSA ($\sim$2630 m^2 g^{-1}), has become an advanced electrode material for SCs. Electrodes made of Graphene have been found to have good reversibility, minimum intrinsic electrical resistivity, and initial solid discharge capacity.[27] Besides these features of rGO, it suffers from agglomeration of layers. To address such challenges, it has been integrated with ABO_3-type perovskite oxides like $LaCo_{1-x}Zn_xO_3$, $Sr_xNi_{1-x}CoO_3$, etc. Therefore, the effectiveness of perovskite-based and rGO-based composite electrode materials for SC applications should be evaluated compared to other materials.

$Sr_{1-x}Ba_xCoO_3$ is an important ABO_3-type perovskite material among the 2D materials family. Herein, Sr and Ba belong to alkaline earth metals occupying the A-site. In contrast, Co belongs to transition metal occupying the B-site as a cation. This type of perovskite has garnered significant attention for its potential applications in SCs due to its favorable

electrochemical properties.[28] This material exhibits high electrical conductivity and a rich redox chemistry, which enhances its capacitance performance. Incorporating barium into the strontium cobalt oxide matrix allows for tunable properties, enabling optimization of ionic conductivity and structural stability. Additionally, the layered perovskite structure of $Sr_{1-x}Ba_xCoO_3$ facilitates efficient ion transport, which is crucial for energy storage applications. Previous research has shown that this material can achieve high specific capacitance and good cycling stability, making it a promising candidate for advanced energy storage technologies. Furthermore, modifying its composition allows researchers to tailor its properties for specific applications in SCs, thus highlighting its significance in energy storage.[10,29]

In this context, Hadji et al. synthesized $LaCo_{1-x}Zn_xO_3$ perovskite-type oxides using the sol–gel method where $LaCo_{0.95}Zn_{0.05}O_3$ exhibits a specific capacitance of 300.47 F g^{-1}, which is around fourfold more significant than that of undoped $LaCoO_3$. Additionally, it demonstrates excellent cycle stability, with 85.73% retention after 5000 cycles. The $LaCo_{0.95}Zn_{0.05}O_3$/activated carbon hybrid device has an ED of 36.12 W h kg^{-1} and retains 81% of its capacitance after 5000 cycles.[30] Shafi et al. prepared $LaMnO_3$ perovskite oxides for SCs in one more study. Conventional synthesis methods conducted at temperatures above 500 °C result in the formation of clumped and deformed structures, which diminish the number of active sites. A sustainable method utilizing natural lemon juice as a surfactant is employed to create three-dimensional polyhedron-structured $LaMnO_3$ nanoparticles (NPs). These NPs exhibit improved specific capacitance and can achieve an ED of up to 52.5 W h kg^{-1} in a symmetric cell arrangement.[31] In another study, Coa et al. prepared $La_{1-x}Sr_xCoO_3$ nanofibers to improve the electrochemical performance of electrode materials for SC. They designed a symmetric and asymmetric device and achieved energy and power densities of about 38 W h kg^{-1} and 400 W kg^{-1}, respectively. Such novel approaches provide a hopeful pathway for developing high-performance SC materials.[32]

This study investigates ABO_3-type perovskite composites, specifically focusing on the $Sr_{1-x}Ba_xCoO_3$ series, with particular emphasis on the $BaCoO_3$ (BCO) variant, which was modified by integrating varying concentrations of reduced graphene oxide (rGO). We employed solvothermal synthesis, a method chosen for its environmental sustainability and effectiveness in yielding composites with robust structural integrity and favorable morphological characteristics. This research primarily explores the transition of capacitor behavior from a basic electric double-layer capacitor (EDLC) to a more complex hybrid capacitor with increasing rGO contents. The BCO-III composites with 15% rGO demonstrated superior electrochemical performance in specific capacity, energy, power densities, and remarkable retention capabilities. Additionally, we quantified diffusion coefficients, transference numbers, ionic conductivity, and relaxation times, providing a comprehensive electrochemical profile of these composites. These results contribute valuable understandings of these materials'

scalability and practical applicability for advanced energy storage systems, highlighting their potential in SC applications.

2. Experimental

2.1 Synthesis of the $Sr_{1-x}Ba_xCoO_3$ by sol–gel auto combustion method

The chemical material required to prepare the complete series of the $Sr_{1-x}Ba_xCoO_3$ (at $x = 0.0$, $x = 0.33$, $x = 0.67$, and $x = 1.0$) were $Sr(NO_3)_2$, $Ba(NO_3)_2$, $Co(NO_3)_2$, CH_4N_2O, and NH_2CH_2-COOH. The appropriate quantities of $Sr(NO_3)_2$ (2.94 g) and $Ba(NO_3)_2$ (2.05 g) were dissolved in 40 mL of deionized water (DIW) in a small beaker. In a separate beaker, 1.315 g of urea and 1.69 g of glycine, serving as fuel agents, were also dissolved in 40 mL of DIW. The molar ratio of the precursor to fuel was adjusted to 2 : 3. After this, all solutions were poured into a beaker to form the collective solution known as a sol. Then, the beaker and the magnetic stirrer were shifted towards the hot plate and stirred for 2 h. As the temperature rose to 95 °C, the beaker began to emit bubbles, indicating the gel formation. The gel continued to thicken due to evaporation and pierced the spin of the magnetic stirrer. When the stirrer was withdrawn, the temperature of the gel had risen to 250 °C, which resulted in self-ignition. After that, the gel-like solution turned into ash. This ash was ground using mortar and pestle to get a fine powder. Then, it underwent calcination at 750 °C for 2 h.

2.2. Preparation of graphene oxide (GO)

A modified Hummers' method was adopted to prepare the GO by oxidizing pure graphite powder. Typically, 25 mL of H_2SO_4 and 4 mL of $NaNO_3$ (volume ratios 1 : 6) were placed into a 200 mL beaker in an ice bath to stir for one h. The mixing solution was then supplemented with 1.0 g of graphite powder while aggressively stirring. The solution turned black because of the graphite powder. Then, 1.32 g of potassium permanganate ($KMnO_4$) was subsequently added to the suspension by keeping the temperature below 20 °C and stirring for 3 h. After stirring, 25 mL of DIW was added dropwise to the reaction system at a temperature lower than 50 °C to start the oxidation. The color of the solution changed to dark brown, which indicated the formation of GO. An additional 100 mL of DIW was added to the solution to further dissolve the graphite and ensure any insoluble material's dispersion. 5 mL of 30% H_2O_2 was steadily added to the solution to remove the unrestricted amount of $KMnO_4$. The solution was washed with 5% HCL to eliminate metal ions and then centrifuged at 450 rpm for 10 min. Conclusively, it was dried in an oven to procure the powder of GO.

2.3 Synthesis of rGO

The solvothermal technique was employed aiming to reduce the GO sheets into rGO. Initially, a precise quantity of 50 mL of undiluted ethanol was wholly combined with a specified amount of GO, which had previously been evenly distributed in water at a 2 mg mL^{-1} concentration. The mixture underwent heating at 70 °C for 3 h and subjected to sonicate for 2 h, followed by 3 h. The mixture was swirled using a magnetic stirrer while maintaining a temperature of approximately 70 °C. Subsequently, the mixture was put into a 100 mL autoclave coated with Teflon. The mixture was then heated for 3 h at 70 °C. The elevated pressure and temperature within the autoclave aided the decrease of GO. After the autoclave reached ambient temperature, the resultant product was gathered. A high-quality, deep-brown powder was acquired after the washing and drying process.
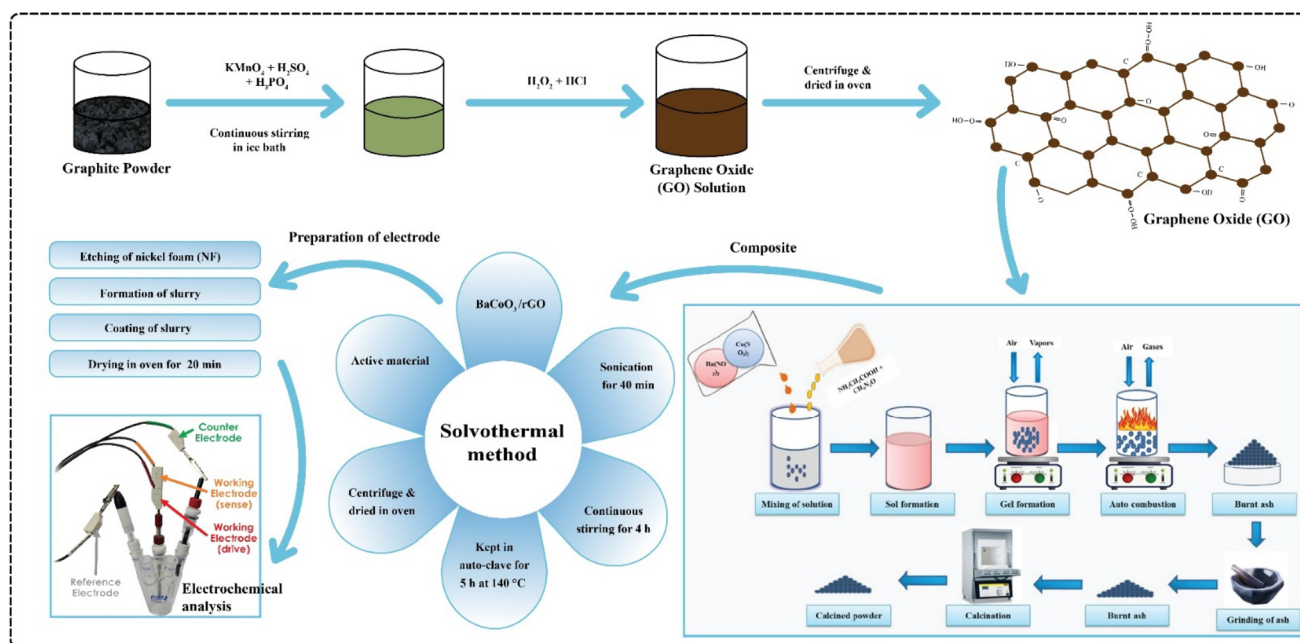

Fig. 1 The schematic profile of sample synthesis.

2.4 Synthesis of the PBCoO$_3$/rGO composites

Four samples were synthesized using a solvothermal method: pure BaCoO$_3$ (PBCO) and BaCoO$_3$ with varying percentages of rGO (5%, 10%, 15%). These samples were labeled PBCO, BCO-I, BCO-II, and BCO-III, respectively. First, PBCO and rGO were united in ethanol and sonicated for 1 h to ensure complete mixing. The solution was stirred using a magnetic stirrer for 4 h. The solution was carefully moved toward a Teflon-lined autoclave after the stirring process. This autoclave was placed inside a muffle furnace and heated at 140 °C for 5 h. After heating, the samples were removed from the autoclave, thoroughly washed to eliminate impurities, and then dried in an oven. This method effectively generates samples.

2.5 Fabrication of electrode

The electrode preparation involved three key steps. Initially, nickel foam (NF) pieces, each measuring 1 × 2 cm, underwent an etching process. This process required immersing the NF in a 50 mL acidic solution, prepared by mixing 13 mL of concentrated H$_2$SO$_4$ with 37 mL of distilled water. Following the etching, the NFs were thoroughly rinsed with distilled water and subsequently dried. To create the binder solution, 10 mL of DMF was combined with 200 mg of PVDF. This mixture was stirred on a hot plate at 150 rpm for 30 min to ensure complete dissolution and uniform mixing. The slurry preparation involved maintaining a precise mass ratio of 8 : 1 : 1 among the active material, the binder solution, and activated carbon. Specifically, the mass of the active material used was 2 mg. The slurry mixture was heated on a hot plate at 450 rpm for 8 h to achieve a homogeneous consistency. Once synthesized, the slurry was uniformly applied to the etched NF. The coated NFs were then transferred to an oven and dried for 30 min to ensure thorough drying and adherence of the slurry to the NFs substrate. These coated NF pieces were then employed as electrodes for further electrochemical analysis in SC applications. The complete procedure of synthesizing the active substance and fabricating the electrode is illustrated in Fig. 1.

3. Results and discussions

In this work, we examined the crystalline structure of the materials using XRD patterns produced by a Bruker D8 advanced X-ray diffractometer using CuK$_\alpha$ radiation (λ = 1.54 Å). We installed a Nova Nano SEM-450 FESEM for a detailed surface study. Additionally, compositional analysis of the samples was done using EDX spectroscopy with an instrument from Oxford. Textural features of prepared samples were revealed via Braunauer–Emmett–Teller (BET) analysis. All electrochemical parameters of the prepared electrodes were tested using a 3-electrode cell system. The experimental setup contained a reference electrode (Ag/AgCl) and a counter electrode (Pt wire) submerged in a 2 M KOH electrolyte. Cyclic voltammetry (CV) curves, electrochemical impedance spectroscopy (EIS), and galvanostatic charge–discharge (GCD) curves were acquired using an electrochemical workstation (CHI 660E).
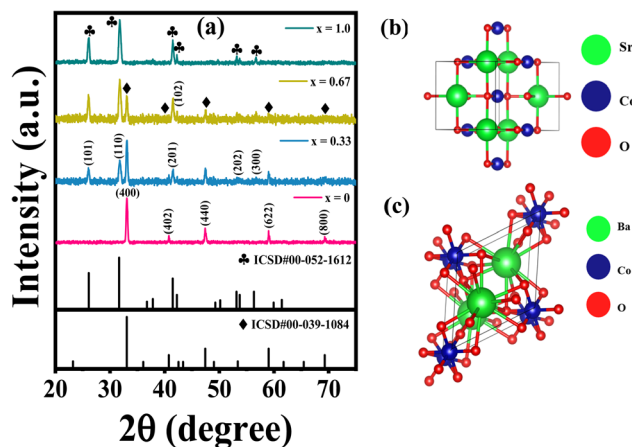

Fig. 2   (a) Standard diffraction and XRD patterns of Sr$_{1-x}$Ba$_x$CoO$_3$ and (b and c) crystal structures of SrCoO$_3$ and BaCoO$_3$.

3.1 Structural analysis

Fig. 2(a) upper panel depicts the standard diffraction patterns along with the experimental XRD pattern of Sr$_{1-x}$Ba$_x$CoO$_3$ samples with compositions $x = 0.0$, $x = 0.33$, $x = 0.67$, and $x = 1.0$. The distinct peaks observed in these XRD patterns confirm the crystalline nature of the samples. For the sample with $x = 0$ (SrCoO$_3$), diffraction peaks are present at 2θ values of 33.10°, 40.70°, 47.43°, 59.01°, and 69.34° corresponding to the crystallographic planes (400), (402), (440), (622) and (800), respectively. This pattern aligns with the tetragonal crystal structure, consistent with the ICSD card no. 00-039-1084, which describes SrCoO$_3$ in the $P\bar{4}mbm$ space group (221). The samples with $x = 0.33$ (Sr$_{0.67}$Ba$_{0.33}$CoO$_3$) and $x = 0.67$ (Sr$_{0.33}$Ba$_{0.67}$CoO$_3$) exhibit diffraction peaks at nearly identical angles to SrCoO$_3$. For the sample with $x = 1.0$ (BaCoO$_3$), diffraction peaks are observed at 2θ values of 25.92°, 31.76°, 41.43°, 42.18°, 53.48°, 56.85° corresponding to the Miller planes (101), (110), (201), (102), (202), and (300) respectively. This pattern confirms a hexagonal crystal structure, in agreement with the ICSD card no. 00-052-1612. The complete substitution of Sr by Ba leads to the transformation from a tetragonal to a hexagonal structure. The XRD patterns of Sr$_{1-x}$Ba$_x$CoO$_3$ thus reveal the crystalline nature of these materials. The SrCoO$_3$ sample exhibits a tetragonal structure, while the BaCoO$_3$ sample demonstrates a hexagonal structure. With the addition of Ba ($x = 0.33$ and $x = 0.67$), peaks of the pure phase (SrCoO$_3$) started to disappear gradually. Upon complete substitution, the crystal structure transitions to a hexagonal phase ($x = 1.0$). The crystal structures of pure samples are shown in Fig. 2(b) and (c).

3.2 Morphological analysis

The morphological features of Sr$_{1-x}$Ba$_x$CoO$_3$ at the substitution of $x = 0$, $x = 0.33$, $x = 0.67$, and $x = 1.0$ were analyzed from SEM images obtained through FESEM, as depicted in Fig. 3(a–d). The images were captured at $10^5\times$ magnification. These analyses were carried out to find the shape and size of the grains present in the samples. Fig. 3(a) shows that at $x = 0$, the sample is
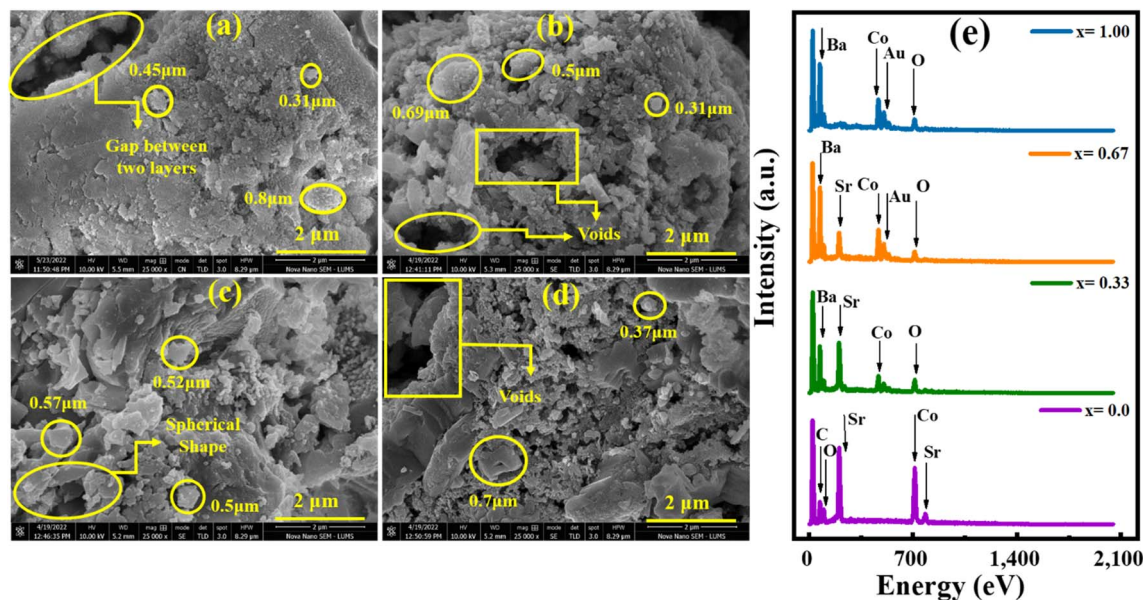
Fig. 3 (a–d) FESEM images of $Sr_{1-x}Ba_xCoO_3$ ($x = 0.00$, 0.33, 0.67, and 1.00) and (e) EDX spectra of $Sr_{1-x}Ba_xCoO_3$ ($x = 0.00$, 0.33, 0.67, and 1.00).

$SrCoO_3$. It is noted that a large number of spherical-size grains with a tiny uniform distribution are present. The sample's average grain size is measured to be 0.52 μm. There are some visible gaps can also be seen. It reveals the small uniform pattern through which ions can easily penetrate. At $x = 0.33$, the sample is $Sr_{0.67}Ba_{0.33}CoO_3$, as shown in Fig. 3(b). It shows that substituting a small amount of Barium (Ba) has transferred its morphology. As the substitution amount is raised, bigger non-uniform grains with clear grain boundaries and an average grain size of 0.5 μm are observed. Some pores can also be seen where the grains are loosely connected. At $x = 0.67$, the sample is $Sr_{0.33}Ba_{0.67}CoO_3$, as represented in Fig. 3(c). By increasing the further substitution of Ba, the grains are closely packed with each other, and the average grain size is found to be 0.53 μm. The porosity and voids have also increased, proving that this sample shows good electrochemical behavior.[9,29] For $x = 1.0$, Fig. 3(d) shows the sample of $BaCoO_3$. The small agglomeration and the presence of voids can also be observed. The average particle size is found to be 0.58 μm. All the microstructures are good porous. Ions can easily be transferred into the electrode's internal structure during the charging and discharging.

3.3. Elemental analysis

EDX spectroscopy was conducted using a Nova Nano SEM 450 scanning electron microscope to ensure the elemental composition of the prepared samples. The EDX analysis verified the presence of Co, O, C, Ba, Sr, and Au, with the detected elemental ratios aligning with the predetermined stoichiometric values. Fig. 3(e) illustrates the EDX spectrum for the composite of $SrCoO_3$ ($x = 0$). In this sample, peaks for Sr and Co are observed, indicating their significant presence. A minor peak for C is also detected, attributed to the carbon adhesive tape used to mount the sample on the aluminum holder. For the sample with $x = $

0.33 ($Sr_{0.67}Ba_{0.33}CoO_3$), the substitution of barium introduces multiple intensity peaks for Ba and O. This diversity arises due to the different characteristic X-rays emitted by a single element.[33] Ba peaks' intensity increases while Sr peaks' intensity decreases, indicating successful barium substitution. The presence of Au results from the gold coating applied to enhance sample conductivity and improve contrast during SEM analysis. As the barium content increases to $x = 0.67$ ($Sr_{0.33}Ba_{0.67}CoO_3$), the EDX spectrum shows further enhancement in the intensity of Ba peaks and a corresponding reduction in Sr peak intensity. Finally, for the sample with $x = 1.0$ ($BaCoO_3$), Ba exhibits the major peaks while Sr peaks are absent, confirming the complete replacement of Sr by Ba. The elements' mol percentage (wt%) values (C, O, Co, Sr, Ba, and Au) were quantified using EDX, as presented in Table S1.† The data indicate a progressive decrease in the mol% of Sr and an associated increase in the mol% of Ba with increasing barium substitution. This corroborates the successful incorporation of Ba into the $SrCoO_3$ lattice and corresponding changes in elemental composition.

3.4. Braunauer–Emmett–Teller (BET) analysis

The textural characteristics of prepared samples were revealed by nitrogen adsorption/desorption isotherms at 77 K, acquired through BET analysis in order to highlight the availability of active sites from specific surface area (SSA), pore size, and volume. Where N_2 gas, due to its inert nature, cost-effectiveness, and high sensitivity (more helpful in the detection of small-sized pores), was used as an adsorbate. According to the IUPAC classification, the displayed N_2 adsorption/desorption isotherms in Fig. 4 are encountered as type IV isotherms, which are characteristics of mesoporous structures and are associated with PBCO, BCO-I, BCO-II, and BCO-III-based samples. Moreover, the low relative pressure region ($P/P_0 <$

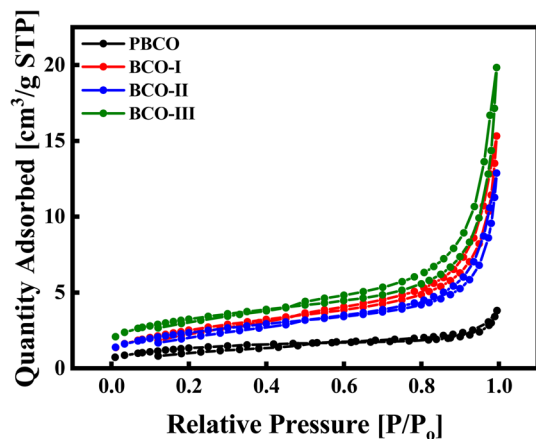$$BaCoO_3^{(4+)} + e^- + H_2O \leftrightarrow BaCoO_3 + OH_{(aq)}^-$$

Fig. 4 Illustration of nitrogen adsorption/desorption isotherms for PBCO, BCO-I, BCO-II, and BCO-III.

0.1) suggests the monolayer coverage that indicates the occupancy of gas molecules to be adsorbed at available surfaces, while the relative pressure region below the 0.9 shows the multilayer coverage of gas molecules due to subsequent layers by Van-der Wall forces. The region right after the multilayer coverage comes the plateau region, indicating the saturation point of multilayer coverage with restricted relative pressure of $P/P_0 > 0.9$ to 1. From Fig. 4, it can be seen that isotherms of BCO-I, BCO-II, and BCO-III showed a clear upward shift due to an increase in SSA attributed 5, 10, and 15% rGO content compared to PBCO at the plateau region. The highest upward shift of BCO-III towards the y-axis suggested the highest adsorbed quantity of nitrogen gas compared to others due to enhanced SSA. Furthermore, the BJH approach opted to calculate the SSA from N_2 adsorption/desorption isotherms for PBCO (4.97 m^2 g^{-1}), BCO-I (9.37 m^2 g^{-1}), BCO-II (8.61 m^2 g^{-1}), and BCO-III (11.64 m^2 g^{-1}), as shown in Table S2.† This analysis confirmed that BCO-III demonstrated fascinating textural features, evidencing its potential as the best electrode material.

3.5 Electrochemical analysis

CV is a fundamental technique employed to investigate the electrochemical characteristics of materials. It enables researchers to comprehend the reactions of substances when the voltage is altered at varying rates, yielding valuable insights into redox mechanisms, electron transport, and capacitive characteristics. During charging, the BaCoO₃ undergoes oxidation by transitioning Co^{3+} to Co^{4+} with the loss of an electron transferred through an external circuit. Using KOH as an electrolyte, the OH^- ions participate,

$$BaCoO_3 + OH_{(aq)}^- \leftrightarrow BaCoO_3^{(4+)} + e^- + H_2O$$
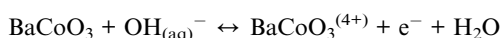
While upon discharging, the transitioning of Co^{3+} to Co^{4+} demonstrates the reversibility by receiving an electron and undergoing the reduction through absorption of OH^- ions from the electrolyte as,
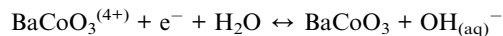
After receiving an electron, $BaCoO_3^{(4+)}$ returns to its original state. $BaCoO_3$ and OH^- ions are released back into the electrolyte, consuming the water.

Fig. 5(a–d) presents the results of CV studies, which comprehensively analyze the charge storage dynamics and capacities of PBCO and its composites. The CV curves, acquired with scan rates ranging from 5 to 100 mV s⁻¹, exhibit clear redox peaks in each cycle. These peaks indicate that the main capacities arise from pseudo-capacitive (PC) and electrical double-layer capacitance (EDLC) behavior, which are associated with faradaic and non-faradaic redox reactions. Even when the scan rates are increased, the continuous symmetrical patterns of the peaks suggest that the charge storage dynamics maintain exceptional cycle reversibility and stability.[34] While minor changes have been observed in the anodic and cathodic peaks, these shifts are caused by polarization effects and do not substantially impact the overall shape of the peaks. The voltammograms obtained for PBCO display voltammograms with rectangular shapes, which are distinctive features of electrochemical behavior beyond simple EDLC. EDLC refers to the storage of charge through electrostatic processes at the electrode surface, resulting in the transfer of non-faradaic charge. In this context, the distinct peaks observed in the voltammograms of PBCO indicate the material's oxidation and reduction processes. The presence of these peaks suggests that the material undergoes reversible redox reactions, contributing to efficient charge storage. However, the CV curves for BCO-I, BCO-II, and BCO-III, depicted in Fig. 5(b–d), demonstrate different characteristics with narrow and low-intensity peaks. This suggests that although both PC and EDLC play a role in the charge/discharge processes, the influence of redox reactions is insignificant, with EDLC being the primary mechanism. The behavior of EDLCs is determined by the aggregation of charges at the interface between the electrode and electrolyte, resulting in the formation of an EDLC. This process is entirely physical, devoid of any chemical processes, and leads to the formation of a bilayer of ions on the surface of the electrode. Materials that demonstrate EDLC often produce a CV curve with a more rectangular form and fewer noticeable peaks than materials with assertive PC behavior. When integrating rGO content into PBCO, a transition from traditional EDLC behavior to hybrid capacitor behavior is observed. This shift is indicated by the combination of capacitive behavior observed in the resultant material. The increased conductivity and significant SSA of rGO play a crucial role in this transition. Consequently, the composite displays attributes resembling EDLCs and PCs, demonstrating hybrid or battery-like properties.

The hybrid nature of rGO arises from its capacity to expedite electron movement and offer an extensive SSA for charge storage, enhancing overall performance and emulating the attributes of battery-type storage.[35,36]

The specific capacity, measured in coulombs per gram (C g⁻¹), quantifies the charge an electrode can store. Eqn (1) performs the calculation.
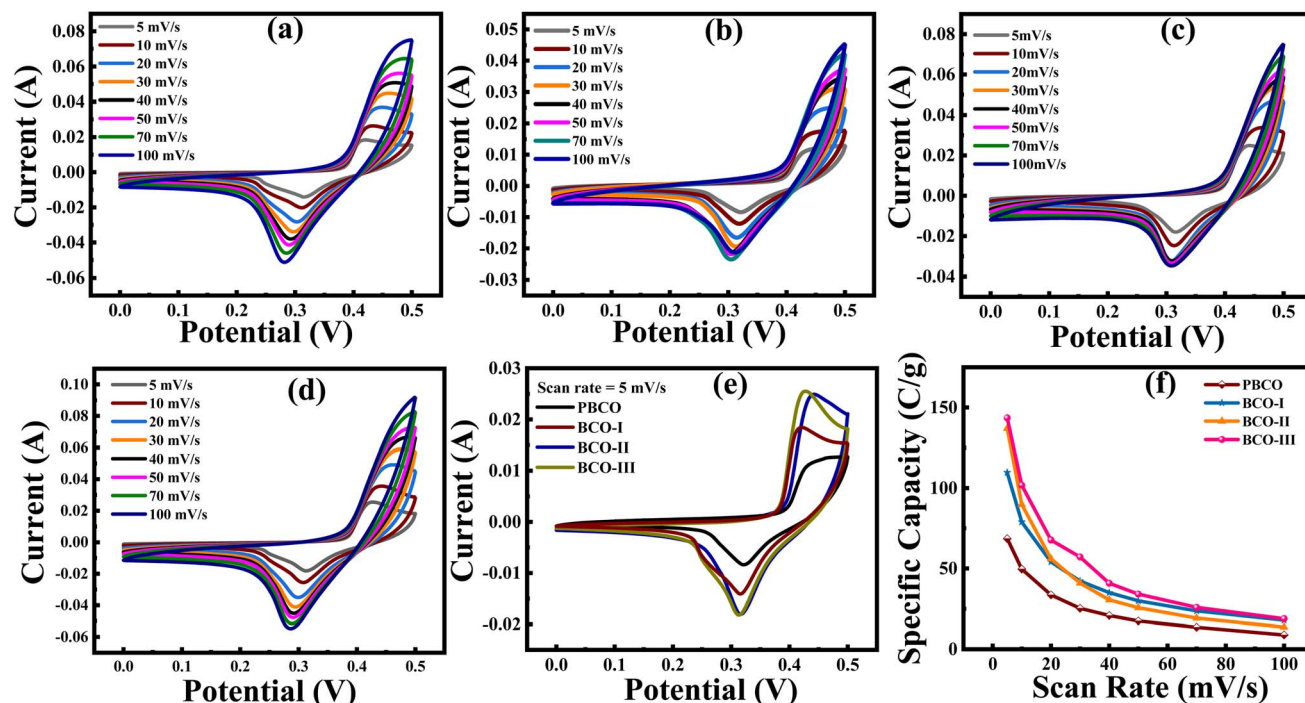
Fig. 5 CV curves at different scan rates for (a) PBCO, (b) BCO-I, (c) BCO-II, (d) BCO-III, and (e) comparison of all samples at 5 mV s^{-1}, and (f) scan rate *vs.* specific capacity.

$$Q_s = \frac{1}{vm} \int_{V_i}^{V_f} I(v)\mathrm{d}V \tag{1}$$

Herein, v and Q_s show the scan rate in millivolts per second (mV s^{-1}) and specific capacity in coulombs per gram (C g^{-1}), while m indicates the loading mass on an electrode, and the integral part denotes the area under the curve.

Table 1 shows that BCO-III has the largest Q_s compared to all other samples, regardless of the scan rates. When the scan rate is set to 5 mV s^{-1}, Q_s reaches its highest value at 143.48 C g^{-1}. The outstanding performance of this material can be due to its highly porous and evenly distributed nanostructure, as evidenced by the FESEM image in Fig. 3(d). The particular Q_s values for each scan rate are shown in Fig. 5(f). As the scan rates increase, there is an evident and expected reduction in the Q_s values. The decrease in performance is attributed to the diminished ability of electrolytic ions to penetrate the electrode material at faster scanning speeds. At higher scanning speeds, only the easily reachable surface sites participate in the transfer of charges, reducing the overall efficiency of the electrochemical process. This occurs because the internal active sites, which contribute substantially to the capacitance at lower scan rates, are not fully utilized.[37] The relationship between scan rates and Q_s highlights the significance of optimizing the electrode's structure and morphology to promote ion accessibility and enhance Q_s, particularly at higher operational speeds. The permeable configuration of BCO-III enables effective ion migration and rapid charge–discharge cycles, which enhances its exceptional efficiency. Nevertheless, decreasing Q_s at higher scan rates emphasizes achieving an optimal SSA and pore structure combination to maximize the material's electrochemical consumption.[15,37]

Based on the transitions mentioned above, the theoretical capacity of a material used in electrochemical cells (such as a battery or hybrid capacitor) is a measure of its potential to store electrical charge, which is governed by the number of charge carriers (electrons or ions) involved in the electrochemical reaction. In this case, we are focusing on the theoretical capacity of BaCoO$_3$ when used in an electrochemical cell in the presence of KOH (potassium hydroxide) as the electrolyte. The theoretical capacity can be determined using Faraday's Law, which relates the total charge Q (in coulombs) transferred during a reaction to the amount of substance that undergoes electrochemical change. The formula for the theoretical capacity is given by,

Table 1 Specific capacity of PBCO, BCO-I, BCO-II, and BCO-III-based electrodes at different scan rates

Specific capacity (C g^{-1})

Scan rate (mV s^{-1})	PBCO	BCO-I	BCO-II	BCO-III
5	68.559	109.676	137.020	143.448
10	49.598	78.932	89.781	101.792
20	33.560	54.111	56.013	67.755
30	25.263	42.233	40.920	57.213
40	20.782	34.980	30.556	40.790
50	17.420	29.916	25.721	34.062
70	13.585	23.659	19.255	25.857
100	8.858	17.916	13.672	18.877

$$Q_{\text{Theoretical}} = \frac{n \times F}{M_w} \quad (2)$$

By applying the formula, we can determine the theoretical capacity of $BaCoO_3$ in C g^{-1}. Given that $n = 1$, $F = 96\,485$ C mol^{-1}, and $M_w = 244.26$ g mol^{-1} is the theoretical capacity in C g^{-1}. Thus, the theoretical capacity of $BaCoO_3$ is approximately 394.77 C g^{-1}.

The experimental capacity of a material is typically lower than its theoretical capacity due to limitations in the electrochemical process, particularly in the ability to fully extract the charge carriers (in this case, potassium ions, K$^+$) from the lattice of the host material. While the theoretical capacity assumes complete extraction of K$^+$ ions, a portion of these ions remains trapped within the lattice structure at higher voltages, significantly above the cut$_{\text{off}}$ potential. This occurs because, as the voltage increases, the interaction between the K$^+$ ions and the host material strengthens, making removing these ions more difficult. The electrochemical reaction slows down, and above a particular potential, the energy required to desolvate further and extract the remaining K$^+$ ions exceeds the applied voltage. As a result, these K$^+$ ions are not accessible for the charge–discharge cycle, limiting the actual capacity of the material. Thus, the difference between theoretical and practical capacity can be attributed to this partial extraction of ions, which is often further exacerbated by side reactions, structural degradation of the material, or inefficient ion transport at higher voltages. Consequently, while the theoretical capacity provides an idealized estimate, the practical capacity reflects the real-world performance of the material, influenced by these electrochemical constraints.

The theoretical framework has been employed to investigate further how electric charge is stored within the gadget to confirm its behavior and contribution. In electrochemical studies, the b-value calculated from Power's law is used to find a sample's charge storage mechanism, as shown in the equation below.

$$i_{\text{peak}} = av^b \text{ or } \log(i_{\text{peak}}) = b\log(v) + \log(a) \quad (3)$$

Herein, a and b are adjustable parameters, representing the intercept and slopes of redox peaks at specific scan rates upon linear fitting using Origin software. Specifically, a, b-value of 0.5 indicates a diffusion-controlled process, while a, b-value of 1 shows a capacitive process. However, a, b-value between 0.5 and 1 suggests that the sample has a hybrid storage mechanism, combining diffusion-controlled and capacitive process elements.[38,39] This mixed behavior indicates that the material can store charge through both faradaic reactions and non-faradaic processes, and this is what we have seen in Fig. 6(a–d). The overall Q_s of energy storage devices are composed of two components: capacitive and diffusive contributions. These components are analyzed via Dunn's model, which is applied to the CV graphs.

$$I(v) = k_1 v + k_2 v^{1/2} \quad (4)$$

Or

$$\frac{i_{\text{peak}}}{v^{0.5}} = k_1 v^{0.5} + k_2 \partial \quad (5)$$

in this context, the symbol $I(v)$ denotes the redox peak currents at a specific scan rate (v). While k_1 and k_2 stand for average slope and intercept values of anodic and cathodic peaks acquired from the linear fitting of $v^{1/2}$ vs. $i_{\text{peak}}/v^{1/2}$ with the help of Origin software, as shown in Fig. 6(e–h). The equation consists of two variables, $k_1 v + k_2 v^{1/2}$, representing distinct factors contributing to the capacitance. The capacitive contribution arises from the electrode resembling a capacitor, involving adsorption and desorption processes. On the other hand, the diffusive contribution originates from the EDLC, involving non-faradaic reactions.

However, Fig. 7 (a–d) shows the samples' combined capacitive and diffusive contributions at multiple scan rates obtained after putting k_1 and k_2 stand for slop and intercept values acquired from the linear fitting of $v^{1/2}$ vs. $i_{\text{peak}}/v^{1/2}$ in eqn (5) at different scan rates, as shown in Fig. 7(a–d) and S2–S5.† The linear graphs Fig. 6(a) and related b-values suggest that the charge storage mechanism is solely controlled by diffusion-
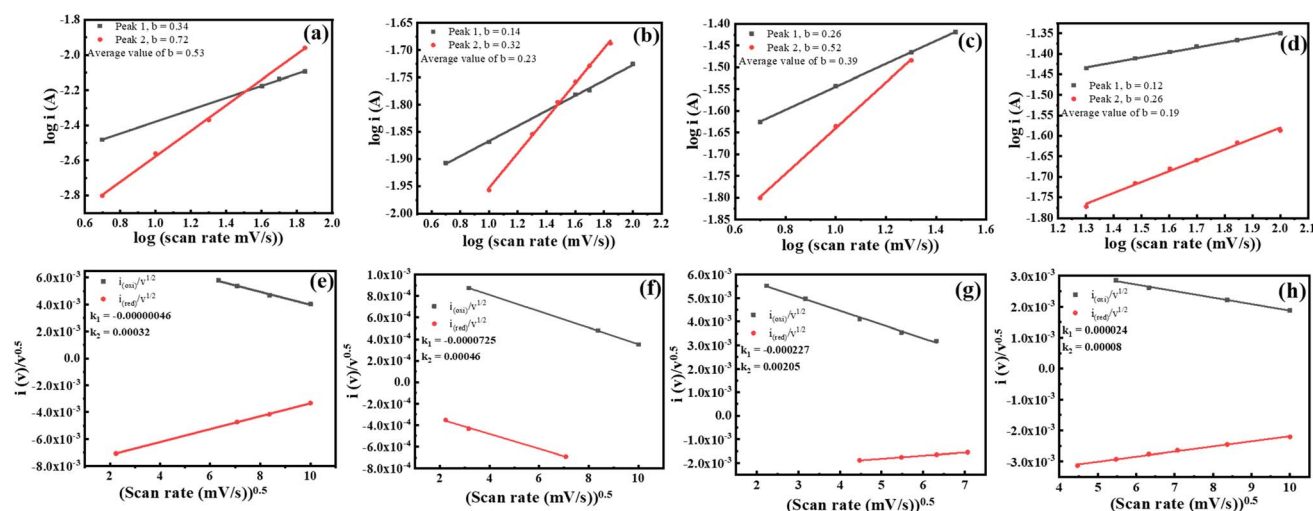

Fig. 6 (a–d) Values of b calculated from the CV curves and (e–h) values of k_1 and k_2 for PBCO, BCO-I, BCO-II, and BCO-III, respectively.

controlled processes, with almost 100% contribution at all scan rates and absence of capacitive behavior. This suggests a robust, non-faradaic process, which is common in materials where the movement of ions plays a crucial role in storing charges. However, Fig. 7 (a–d) exhibits a combination of diffusion-controlled and capacitive processes that collectively contribute to the overall charge storage. At lower scan speeds (where $v = 5$ mV s^{-1}), the diffusion-controlled contribution accounts for 80% of the total charge storage, while the capacitive contribution makes up 20%. This dominance of diffusion-controlled processes at low scan rates can be attributed to the effective diffusion of ions in the electrolyte, allowing them to interact with the electrode surface fully. With the scan rate increasing, the capacitive contribution reaches 44% when $v = 50$ mV s^{-1}, while the diffusion-controlled contribution decreases to 56%. This shift implies that at higher scan speeds, the rapid charge–discharge cycles limit the time available for ion diffusion, thus enhancing the contribution of capacitive processes. The faster capacitive processes are favored as they rely on the immediate response of the electrode material to the applied voltage rather than the slower diffusion of ions. Including rGO further influences the observed behavior in Fig. 7(b); due to its excellent electrical conductivity, rGO facilitates rapid electron transfer, thereby enhancing the capacitive response of the electrode. This conductive nature of rGO and its high SSA and porous structure contribute to the hybrid capacitor behavior, as observed in Fig. 7(a–d). The Fig. 7(c) shows a notable rise in capacitive behavior with increasing scan rates. Initially, at $v = 5$ mV s^{-1}, the diffusion-controlled contribution is 74%, and the capacitive contribution is 26%. At $v = 50$ mV s^{-1}, these contributions shift

to 47% and 53%, respectively, indicating a near equilibrium. This shows the enhanced capacitive response at higher scan rates and the importance of ion diffusion at lower rates, showcasing the system's efficient charge storage capabilities across varying conditions. Fig. 7(d) shows the highest capacitive contributions among the figures. At $v = 5$ mV s^{-1}, the diffusion-controlled contribution is 60%, and the capacitive contribution is 40%. As the scan rate increases to $v = 50$ mV s^{-1}, the capacitive contribution surges to 68%, while the diffusion-controlled contribution drops to 32%. This significantly shifts towards capacitive storage mechanisms at higher scan rates, emphasizing the material's ability to transition from non-faradaic to faradaic behavior.

Fig. 7 confirms that faradaic and non-faradaic processes affect the device's electrochemical performance. It concisely depicts the capacitive and diffusive control elements included in the device. Fig. 7(e) shows that the capacitive-controlled division significantly increases with the increase in scan rate. In contrast, Fig. 7(f) shows a significant decrease in the diffusive-controlled fraction under comparable conditions.[37]

In a nutshell, PBCO exhibits prominent EDLC behavior due to its substantial redox activity. In contrast, BCO-I, BCO-II, and BCO-III predominantly display hybrid behavior, encompassing EDLC and PC behaviors. As the concentration of rGO increases, the materials shift towards a more hybrid capacitive behavior. It can be observed by modifying peaks and alterations in their electrochemical behavior while maintaining a restricted amount of redox activity. The variability in the behavior of these materials directly impacts the performance and utilization of these materials in energy storage devices.
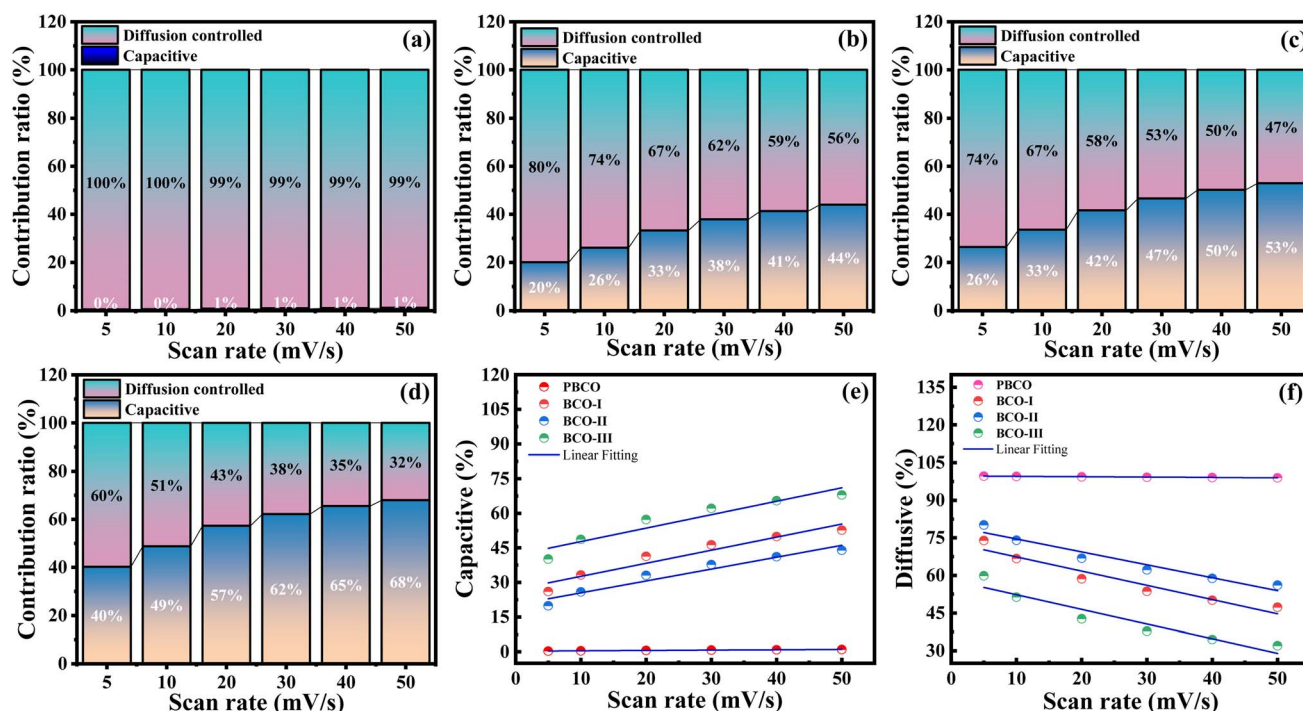

Fig. 7 (a–d) Ratios of capacitive and diffusive controlled process, (e) capacitive *vs.* scan rate, and (f) diffusive *vs.* scan rate, for PBCO, BCO-I, BCO-II, and BCO-III, respectively.

An electrode material's electrochemical surface area (ECSA) describes the active sites facilitating redox activity. It is usually measured through double-layer capacitance (C_{dl}) from the non-faradaic mechanism region, where no current change due to potential variation is observed. In our case, this region is observed between 0.01 V and 0.08 V, as depicted in Fig. S1(a–d)† for all samples, indicating the values of C_{dl} from the slope after linear fitting of scan rate *vs.* current densities ($\Delta J = (J_a - J_c)/2$) at multiple scan rates.[40] The eqn (6) has been used to quantify the ESCA.

$$\mathrm{ECSA} = \frac{C_{dl}}{C_{sp}} \qquad (6)$$

Eqn (6) helps calculate the ECSA of PBCO, BCO-I, BCO-II, and BCO-III-based electrode materials to be 7.45, 3.80, 7.10, and 10.10 cm^2, respectively.

GCD testing, also known as constant current charge–discharge, is a fundamental electrochemical technique employed to characterize the performance of energy storage devices, such as SCs and batteries. Fig. 8(a–d) depicts the GCD profiles of PBCO$_3$ and its composites obtained at 5 to 50 mA. Each graph illustrates the voltage response over time for both the charging and discharging cycles. The curves demonstrate a notable level of symmetry, suggesting exceptional electrochemical reversibility and stability. The duration of both charging and discharging cycles reduces with increased current density, indicating a faster rate of electrochemical reactions at higher currents. Fig. 8(e) depicts the correlation between Q_s in C g^{-1} and current density (A g^{-1}) for PBCO and its composites. It

has been noted that the value of Q_s falls as the current density increases in all samples. This is a common occurrence caused by the shorter time for ion diffusion at higher current densities. However, adding rGO greatly improves the conductivity at all electric current levels.[41] BCO-III exhibits the highest Q_s, followed by samples BCO-I and BCO-II. To calculate Q_s, PD, and ED following equations were used;

$$Q_s = \frac{I \times \Delta t}{m} \qquad (7)$$

$$E(\mathrm{W\ h^{-1}\ kg^{-1}}) = \frac{\Delta V \times Q_s}{2 \times 3.6} \qquad (8)$$

$$P(\mathrm{W\ kg^{-1}}) = \frac{E \times 3600}{\Delta t} \qquad (9)$$

In eqn (7), the variables m and Q_s represent the mass of the electrode material and specific capacity in coulombs per gram (C g^{-1}), while I and Δt reflect the current in amperes (A) and discharge time. A lengthier discharge duration signifies a superior capacity for charge storage in the electrode. Table 2 lists all the calculated values of discharge capacitance, ED, and PD, while Table 3 compares these results with previously reported data.[42–49]

Fig. 8(f) displays the Ragone plot, illustrating the correlation between ED and PD for the samples. The plot demonstrates that the addition of rGO not only increases the Q_s but also enhances the ED of the materials. To evaluate the performance of the electrode, we conducted an extensive cyclic stability test on BCO-III, performing 5000 charge–discharge cycles at a current of 5 mA. The result in Fig. 9 indicates that BCO$_3$-III has an
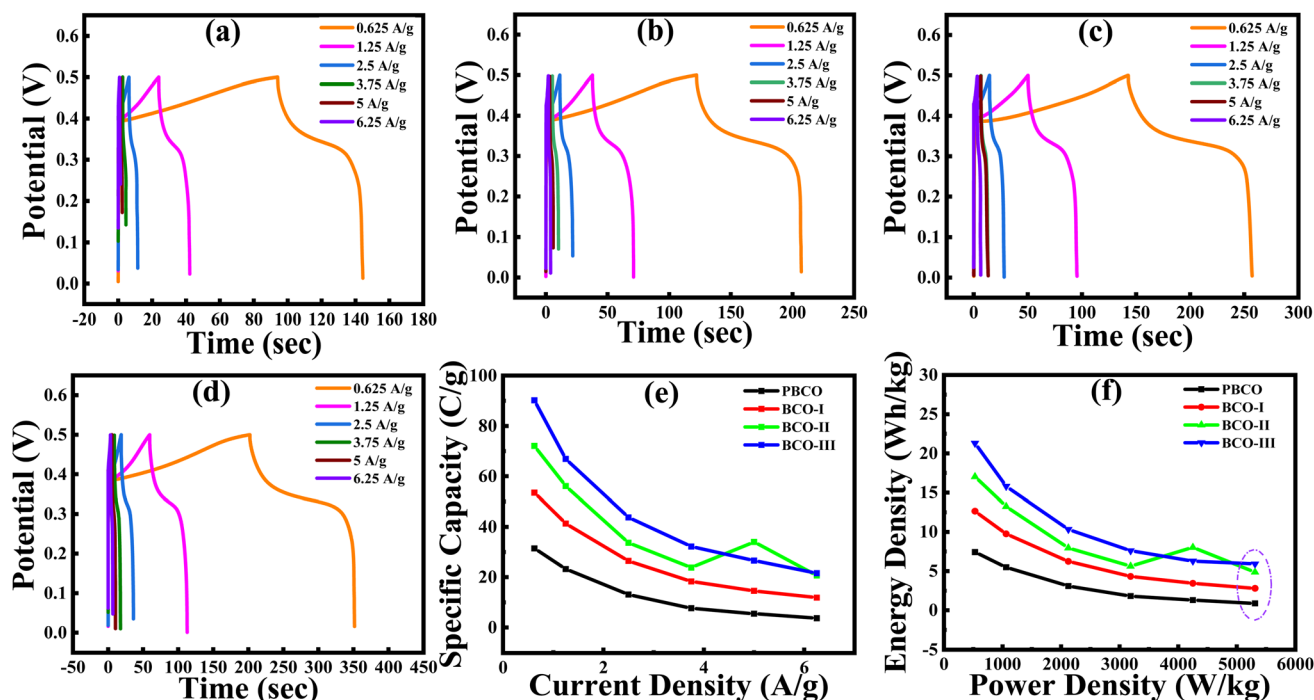

Fig. 8 GCD curves at different current densities for (a) PBCO, (b) BCO-I, (c) BCO-II, (d) BCO-III, and (e) current density *vs.* specific capacity, and (f) power density *vs.* energy density.

Table 2 Specific capacity, energy density, and power density of PBCO, BCO-I, BCO-II, and BCO-III

Sample	Current density ($A\ g^{-1}$)	Discharging time (s)	Specific capacity ($C\ g^{-1}$)	Energy density ($W\ h\ kg^{-1}$)	Power density ($W\ kg^{-1}$)
PBCO	0.62	50.27	31.41	7.41	531.25
	1.25	18.60	23.25	5.49	1062.5
	2.50	5.24	13.10	3.09	2125
	3.75	2.04	7.65	1.29	3187.5
	5.00	1.09	5.48	1.80	4250
BCO-I	6.25	0.59	3.68	0.87	5312.5
	0.62	85.61	53.50	12.63	531.25
	1.25	33.03	41.29	9.75	1062.5
	2.50	10.58	26.45	6.24	2125
	3.75	4.88	18.29	4.32	3187.5
	5.00	2.91	14.55	3.43	4250
	6.25	1.89	11.85	2.79	5312.5
BCO-II	0.62	115.30	72.06	17.01	531.25
	1.25	44.87	56.08	13.24	1062.5
	2.50	13.47	33.67	7.95	2125
	3.75	6.35	23.81	5.62	3187.5
	5.00	6.80	34.01	8.02	4250
	6.25	3.30	20.62	4.87	5312.5
BCO-III	0.62	144.25	90.15	21.28	531.25
	1.25	53.49	66.86	15.78	1062.5
	2.50	17.50	43.75	10.33	2125
	3.75	8.58	32.17	7.59	3187.5
	5.00	5.32	26.60	6.28	4250
	6.25	3.45	21.56	5.91	5312.5

impressive lifespan, retaining 90% of its initial capacity after 5000 cycles and demonstrating a remarkable coulombic efficiency of 94%. This excellent retention can be attributed to the inclusion of rGO within the BCO-III matrix and the practical synthesis achieved through the solvothermal process. The presence of rGO enhances the structural integrity and electrical conductivity of BCO-III, thereby improving its durability and performance during repeated cycling. Additionally, the solvothermal synthesis method ensures a homogeneous distribution of rGO within the matrix, contributing to the overall stability and efficiency of the electrode. This stability under prolonged cycling demonstrates the potential of BCO-III for use in high-performance energy storage devices.[50]

EIS measurements were performed across a frequency spectrum of 10^{-2} to 10^5 Hz to elucidate the ion diffusion and electron transfer characteristics. Fig. 10 depicts the resultant

Nyquist plots and the equivalent circuit model derived from the EIS data. The Nyquist plots depict the correlation between the imaginary component of impedance (Z'') and the fundamental element of impedance (Z'). They provide insights into the resistance and capacitive properties of the electrode materials.[51]

The Nyquist plot of PBCO, as seen in Fig. 10(a), displays a prominent semicircle, which signifies a higher charge transfer resistance (R_{ct}). This indicates that PBCO has a poorer conductivity and lacks sufficient charge transfer at the contact between the electrode/electrolyte interface. When rGO is added at a low concentration (BCO-I), as depicted in Fig. 10(b), the diameter of the semicircle reduces slightly, suggesting a moderate decrease in R_{ct}. This may be attributed to enhanced conductivity optimization arising from the effective dispersion of rGO. When the concentration of rGO reaches a moderate level (BCO-II), as seen in Fig. 10(c), the diameter of the

Table 3 Comparison of electrochemical parameters of different related materials

Sample	Specific capacitance ($F\ g^{-1}$)	Energy density ($W\ h\ kg^{-1}$)	Power density ($W\ kg^{-1}$)	Cyclability (%)	References
CoO_3/MWCNTs	202	25	900	—	42
$LaCoO_3$/rGO	317	—	—	75% after 5k cycles	43
$SrCoO_3$	303	—	—	50% after 10k cycles	44
NiO/rGO	171.3	—	—	20% after 2k cycles	45
CuS/rGO	235 $C\ g^{-1}$	43	1426	95% after 2k cycles	46
Ta substituted $SrCoO_3$	227.91 $C\ g^{-1}$	22.82	775.09	90% after 5k cycles	47
Fe substituted $SrCoO_3$	526.6	26.2	800	86% after 5k cycles	48
rGO/TiO_2	15.02	2.58	4000	—	49
$BaCoO_3$/rGO	90.15 $C\ g^{-1}$	21.28	531	90% after 5k cycles	This work
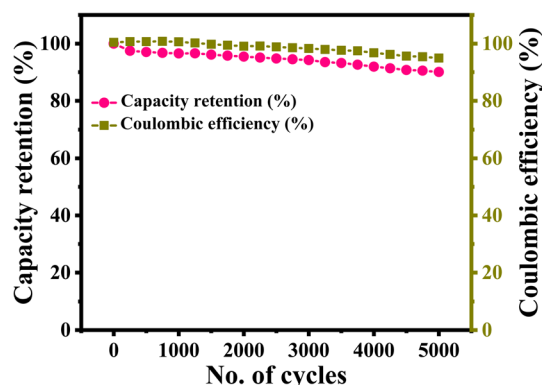
Fig. 9 Cyclic stability of BCO-III at 5 mA after 5000 cycles.

Table 4 Relaxation time calculated from the Bode plot

Sample	Phase angle (degree)	Frequency (Hz)	$\tau = \dfrac{1}{2\pi f_c}$ (seconds)
PBCO	497	0.54	0.31
BCO-I	65	177	0.089
BCO-II	70	0.083	0.13
BCO-III	42.4	2.88	0.055

semicircle shrinks even further. This indicates a lower R_{ct} compared to BCO-I. At modest quantities of rGO, the material is likely to be well dispersed, which improves the mobility of electrons and reduces resistance. Fig. 10(d) represents the highest concentration of rGO (BCO-III). At this concentration, the semicircle is the shortest, which suggests the most favorable R_{ct}. The notable reduction in R_{ct} is due to the elevated concentration of rGO, which results in enhanced conductivity and charge transfer efficiency.[52]

The linear segments observed at low frequencies in the Nyquist plots indicate the Warburg impedance, which is linked to the diffusion of ions in the electrolyte. The significant reduction in the slope seen in the BCO-III linear zone indicates remarkable ion transport, providing additional proof of rGO's

enhancement of electrochemical performance.[53] Biologic EC Lab V11.6 was used to measure all EIS parameters, as listed in Table 5.

Moreover, we calculated the relaxation time for different materials based on the Bode plot of the frequency phase relationship, as depicted in Fig. 10(e). This relaxation time indicates how long a SC returns to normal after distraction. It measures energy dissipation and is linked to the SC's internal resistance. A longer relaxation time means elevated internal resistance, which can reduce the SC's ability to deliver power efficiently. For the BCO-III composite, the relaxation time is 0.055 s, which is significantly lower than that of PBCO, BCO-I, and BCO-II.[54] Table 4 presents the calculated values of relaxation time from the Bode plot.

3.6. Diffusion coefficient

To evaluate the electrochemical behavior of the prepared samples with KOH as the electrolyte, their diffusion coefficients were determined using eqn (10).
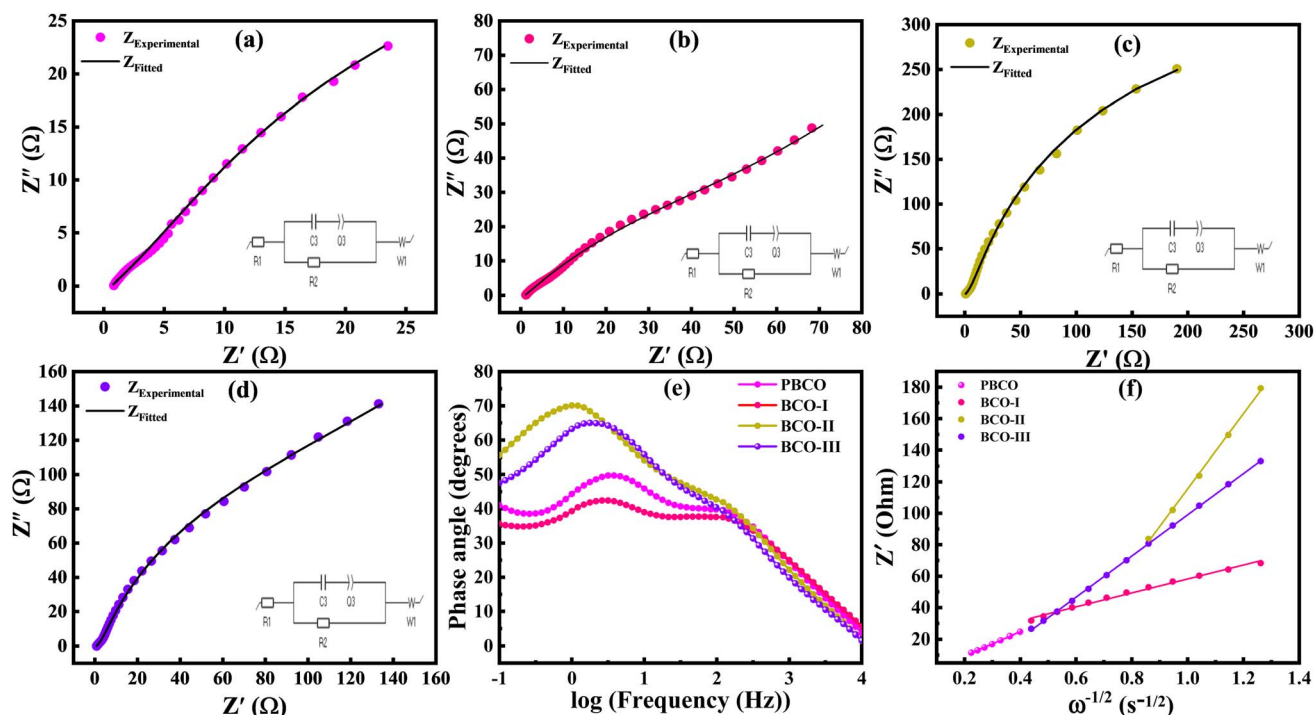

Fig. 10 (a–d) EIS circuit fitting spectra for PBCO, BCO-I, BCO-II, and BCO-III, respectively, (e) Bode plot for all the prepared samples (f) Warburg coefficients from linear fitting between $\omega^{-1/2}$ vs. real part of impedance for all the prepared samples.

Table 5 Parameters obtained from EIS measurements of PBCO, BCO-I, BCO-II, and BCO-III

Sample	R_s (Ω)	R_{ct} (Ω)	C_3 (F)	D_{K}^{1+} (cm^2 s^{-1})	δ (Ω s$^{-1/2}$)	σ (S cm^{-1})	Transference number (t_+)
PBCO	0.94	0.0116	0.17	1.56×10^{-15}	238.40	0.0841	0.20
BCO-I	0.73	0.0114	0.023	5.16×10^{-15}	130.93	0.110	0.22
BCO-II	0.68	0.007	0.0051	1.53×10^{-14}	76.01	0.118	0.22
BCO-III	0.62	0.003	0.0048	4.51×10^{-14}	44.36	0.129	0.20

$$D^{\text{EIS}}/K^{+1} = \frac{R^2 T^2}{2 \times A^2 \times n^4 \times F^4 \times c^2 \times \delta^2} \quad (10)$$

Here, D^{EIS}/K^{+1} stands for diffusion coefficient calculated from EIS spectrum using KOH electrolyte, R and T reflect the real gas constant (8.31 mol^{-1} K^{-1}) and absolute temperature of about 298 K, and A is the surface area of an electrode (0.5 cm^2). N is the number of electrons that participate in redox activity. At the same time, F, c, and δ are the Faraday constant, the concentration of electrolytic species at the electrode surface, and the Warburg coefficient obtained from linear fitting of low-frequency region *vs.* the real part of the impedance, suggesting that the diffusion coefficient is inversely proportional to the square of the Warburg coefficient. Therefore, higher δ values will reflect the slower diffusion dynamics and *vice versa* for lower δ values. Moreover, the low value of this coefficient reflects the ion's mobility due to enhanced acceleration toward their migration from the electrode to the electrolyte and *vice versa* due to well-structured materials providing short diffusion pathways, suggesting a significant decrease in resistance. In our case, the gradual decline in the Warburg coefficient is associated with elevated content of rGO, evidencing the improved conductivity with reduced resistance. While the value of c reflects the electrolyte concentration at the electrode surface, it has been determined using the Nernst equation, which is generalized into eqn (11).

$$E = E^0 + \frac{RT}{nF} \ln \frac{C_{\text{surface}}}{C_{\text{bulk}}} \quad (11)$$

The Nernst equation can be generalized into eqn (12).

$$C_{\text{surface}} = C_{\text{bulk}} \times e^{\left(\frac{nF(E-E^\circ)}{RT} \right)} \quad (12)$$

Herein, C_{surface} highlights the amount of electrolyte concentration at the electrode surface. C_{bulk} indicates the total concentration of electrolyte ions, and $E - E^\circ$ showcases the potential difference between the applied and standard. On the other hand, n stands for the number of electrons transferred, and F is for Faraday's constant. Meanwhile, R and T are the real gas constants, respectively. Diffusion coefficients for PBCO, BCO-I, BCO-II, and BCO-III were measured as 1.56×10^{-15}, 5.16×10^{-15}, 1.53×10^{-14}, and 4.51×10^{-14} cm^2 s^{-1}, respectively.

The diffusion coefficient plays a vital role in the electrochemical performance of materials. A higher diffusion coefficient typically correlates with better electrochemical performance, implying faster ion transport within the electrolyte, leading to more efficient redox reactions at the electrode

surface. This efficiency is crucial for applications such as batteries, supercapacitors, and fuel cells, where the rate of ion transport can significantly affect the overall device performance. For instance, BCO-III, with the highest diffusion coefficient, would likely exhibit the best electrochemical performance among the samples studied, making it a promising candidate for applications where rapid ion transport is necessary. On the other hand, BCO-II, with the lowest diffusion coefficient, may suffer from slower reaction kinetics, potentially limiting its performance in similar applications. Fig. 10(f) shows the linear relationship between $\omega^{-1/2}$ and Z' in the low-frequency region of the Nyquist plots, resulting in the Warburg coefficient (δ) obtained from slop for all prepared samples listed in Table 5. Moreover, the more significant value of δ is indicative of poorer diffusion, and lower reflects the efficient ion diffusion; that's what we have estimated for PBCO to be approximately 238.40 Ω s$^{-1/2}$ and for BCO-III to be 44.36 Ω s$^{-1/2}$, suggesting that BCO-III proved to be a potential candidate for good electrochemical performance.[55–58]

3.7. Ionic conductivity (σ)

In supercapacitor technology, ionic conductivity is a crucial parameter that helps us determine a material's electrochemical efficiency. Table 5 lists the estimated ionic conductivity values for PBCO, BCO-I, BCO-II, and BCO-III. The values of ionic conductivities for all samples have been determined using eqn (13).

$$\sigma = \frac{L}{R_i \times A} \quad (13)$$

Herein, σ is the ionic conductivity, L & A are the thickness and surface area of the electrode, and R_i is the solution (series) resistance. The ionic conductivities in Table 5 for PBCO, BCO-I, BCO-II, and BCO-III show an increasing trend with adding rGO content to PBCO. The highest 0.128 S cm^{-1} for BCO-III has been calculated, suggesting the best electrode material.

3.8. Transference number (t_+)

From the transference number, we can deduce the contributions of the cation and anion to the overall current within the system. In ionic conduction, not all ions may contribute equally to the current. The transference number allows us to quantify the fraction of the current carried by each ion type. For this purpose, the following equation has been used as,

$$t_+ = \frac{1}{1 + Z_d(0)/R_b} \quad (14)$$

Here, R_b is the electrolyte resistance, and Z_d (0) is the impedance at low frequency due to Warburg diffusion. In this experiment, the transference number for the cation (t_+) is observed to be 0.22. Since the sum of the transference numbers for cations and anions equals 1 ($t^+ + t^- = 1$), knowing the transference number of one ion enables us to determine the other. For instance, a transference number of 0.2 for the cation implies a transference number of 0.8 for the anion, indicating that anions carry a more significant portion of the current. In practical terms, if most of the current is carried by cations, the concentration gradient formed at the electrode during charging will be smaller, potentially reducing polarization effects. Conversely, when the transference number of the cation is low, as in this case, the concentration gradient at the electrode increases, which can limit the charging rate of the system due to the buildup of ions at the electrode interface.[59] Thus, adjusting the transference number can be essential for optimizing charge transport and improving the efficiency of the system's charging process. The transference numbers for all samples have been tabulated in Table 5.

4. Conclusion

The synthesis of $BaCoO_3$/rGO composites (specifically PBCO, BCO-I, BCO-II, and BCO-III) *via* a solvothermal technique, followed by Ni foam etching, cleansing, and slurry creation, has shown substantial promise in addressing global energy challenges. Phase development was verified using XRD, with Bragg's plane (hkl) values aligning with the provided data and ICSD ID # 00-052-1612. FESEM analysis revealed nanoscale structures that were uniformly distributed and exhibited high porosity. Electrochemical analysis indicated a transition from electric double-layer capacitance (EDLC) to a combination of capacitive behaviors, with the BCO-III composite achieving an impressive specific capacity of 142.44 C g^{-1} at a scan rate of 5 mV s^{-1}. Although the presence of surface species leads to a decline in specific capacity at higher scan rates, BCO-III demonstrates excellent discharge rates, power density (531.25 W kg^{-1}), and energy density (21.28 W h kg^{-1}). The sample BCO-III, which had the highest specific capacity, was tested for stability and showed an impressive retention rate of 90%. Further, excellent ionic conductivity confirmed the highlighted features of BCO-III. The cation's transference number is determined to be 0.2, indicating that the anion will undergo a large current. These properties highlight its potential as a high-performance electrode material for SCs and other energy storage applications.

Data availability

The data will be made available upon request.

Conflicts of interest

There are no conflicts to declare.

References

1 M. Hasan, S. Zawar, G. M. Mustafa, A. Ghaffar, A. Razaq and S. Atiq, Porous Architecture of Ni substituted $ZnMn_2O_4$ nanospheres as an electrode material for supercapacitor applications, *Phys. B*, 2022, **633**, 413767.

2 M. Walter, M. V. Kovalenko and K. V. Kravchyk, Challenges and benefits of post-lithium-ion batteries, *New J. Chem.*, 2020, **44**(5), 1677–1683.

3 A. P. Tiwari, T. Mukhiya, A. Muthurasu, K. Chhetri, M. Lee, B. Dahal, *et al.*, A review of electrospun carbon nanofiber-based negative electrode materials for supercapacitors, *Electrochem*, 2021, **2**(2), 236–250.

4 B. Talluri, K. Yoo and J. Kim, High entropy spinel metal oxide $(CoCrFeMnNi)_3O_4$ nanoparticles as novel efficient electrocatalyst for methanol oxidation and oxygen evolution reactions, *J. Environ. Chem. Eng.*, 2022, **10**(1), 106932.

5 Q. Ma, H. Liu, S. An, X. Han, J. Cui, Y. Zhang, *et al.*, Layered double metal hydroxide coated nickel oxide embedded carbon fiber to form open petal-shaped nanosheet arrays as electrode materials for high-performance supercapacitors, *J. Energy Storage*, 2021, **44**, 103455.

6 Y. Niu, H. Su, X. Li, J. Li and Y. Qi, Synthesis of porous α-MoO_3 microspheres as electrode materials for supercapacitors, *J. Alloys Compd.*, 2022, **898**, 162863.

7 X. Mao, Y. Zou, F. Xu, L. Sun, H. Chu, H. Zhang, *et al.*, Three-dimensional self-supporting Ti_3C_2 with MoS_2 and Cu_2O nanocrystals for high-performance flexible supercapacitors, *ACS Appl. Mater. Interfaces*, 2021, **13**(19), 22664–22675.

8 S. Wang, Y. Zou, F. Xu, C. Xiang, H. Peng, J. Zhang, *et al.*, Morphological control and electrochemical performance of $NiCo_2O_4$@ NiCo layered double hydroxide as an electrode for supercapacitors, *J. Energy Storage*, 2021, **41**, 102862.

9 Z. Yu, S. Wang, Y. Huang, Y. Zou, F. Xu, C. Xiang, *et al.*, Bi_2O_3 nanosheet-coated $NiCo_2O_4$ nanoneedle arrays for high-performance supercapacitor electrodes, *J. Energy Storage*, 2022, **55**, 105486.

10 X. Yang, C. Xiang, Y. Zou, J. Liang, H. Zhang, E. Yan, *et al.*, Low-temperature synthesis of sea urchin-like Co-Ni oxide on graphene oxide for supercapacitor electrodes, *J. Mater. Sci. Technol.*, 2020, **55**, 223–230.

11 L. Tan, D. Guo, J. Liu, X. Song, Q. Liu, R. Chen, *et al.*, In-situ calcination of polyoxometallate-based metal organic framework/reduced graphene oxide composites towards supercapacitor electrode with enhanced performance, *J. Electroanal. Chem.*, 2019, **836**, 112–117.

12 W. Song, X. Ma, L. Qiu, R. Guo, X. Lu and B. Sun, Anchoring polyaniline nanofibers on liquefied wood carbon aerogel for high-performance hybrid supercapacitors, *Ind. Crops Prod.*, 2024, **215**, 118645.

13 Y. Wang, Nanowire materials for supercapacitor electrode: Preparation, performance and prospects, *J. Energy Storage*, 2024, **97**, 112848.

14 J. Wang, X. Zhang, Z. Li, Y. Ma and L. Ma, Recent progress of biomass-derived carbon materials for supercapacitors, *J. Power Sources*, 2020, **451**, 227794.

15 T. N. Myasoedova, O. V. Nedoedkova, R. Kalusulingam, Y. V. Popov, A. S. Mikheykin, A. S. Konstantinov, *et al.*, Fabrication of Ni-Polyaniline/Graphene Oxide Composite Electrode with High Capacitance and Water Splitting Activity, *ChemPhysChem*, 2024, **25**(15), e202300795.

16 F. Yang, H. Guo, J. Zhang, Y. Cao, Y. Chen, J. Xu, *et al.*, Heterostructure of $MnCo_2O_4$ intercalated graphene oxide coated with Ni–V–Se nanoparticles for supercapacitors with high rate capability, *J. Alloys Compd.*, 2022, **926**, 166762.

17 P. K. Sahoo, N. Kumar, A. Jena, S. Mishra, C. P. Lee, S. Y. Lee, *et al.*, Recent progress in graphene and its derived hybrid materials for high-performance supercapacitor electrode applications, *RSC Adv.*, 2024, **14**(2), 1284–1303.

18 R. Kumar, R. Thangappan, F. Ran, S. Sambasivam, M. D. Albaqami and S. Mohammad, Enriched performance of practical device assisted asymmetric supercapacitor: NiO/Co_3O_4 intercalated with rGO nanocomposite electrodes, *J. Energy Storage*, 2024, **85**, 111075.

19 S. A. Thomas, J. Cherusseri and D. N. Rajendran, Recent advancements on carbon fibers-based sustainable electrodes for flexible and wearable supercapacitors, *RSC Sustainability*, 2024, **2**, 2403–2443.

20 K. Mariappan, D. D. F. Packiaraj, T. W. Chen, S. M. Chen, S. Sakthinathan, S. Alagarsamy, *et al.*, The electrochemical performances of porous niobium pentoxide with multi-walled carbon nanotubes nanocomposite incorporated with glassy carbon electrode for the sensing of chloramphenicol, *Colloids Surf., A*, 2024, **691**, 133840.

21 S. S. Shah and M. A. Aziz, Properties of Electrode Materials and Electrolytes in Supercapacitor Technology, *J. Chem. Environ.*, 2024, **3**(1), 1–45.

22 J. Duan, J. Li, G. Divitini, D. Cortecchia, F. Yuan, J. You, *et al.*, 2D hybrid perovskites: from static and dynamic structures to potential applications, *Adv. Mater.*, 2024, **36**(30), 2403455.

23 S. Ali, A. Shakoor, M. Raza and A. Ahmad, Facile Synthesis of Zinc Cobalt Sulfide and Composite with Graphitic Carbon Nitride (ZCS@ GCN) for Photocatalysis and Electrode for Energy Storage Applications, *Mater. Chem. Phys.*, 2025, 130431.

24 P. J. Sephra, T. Chandrapagasam, A. Sachdev and M. Esakkimuthu, Bifunctional properties of $Ag/\alpha-Fe_2O_3/$ rGO nanocomposite for supercapacitor and electrochemical nitrate sensing using tetradodecyl ammonium nitrate as ion-selective membrane, *Environ. Sci. Pollut. Res.*, 2024, **31**(40), 52886–52904.

25 X. T. Yin, E. M. You, R. Y. Zhou, L. H. Zhu, W. W. Wang, K. X. Li, *et al.*, Unraveling the energy storage mechanism in graphene-based nonaqueous electrochemical capacitors by gap-enhanced Raman spectroscopy, *Nat. Commun.*, 2024, **15**(1), 5624.

26 M. Peplow, Coming of age, *Science*, 2024, **386**, 138–143.

27 J. B. Falqueto, N. Hales, T. J. Schimidt and E. Fabbri, Recent Advances in Nickel-Based Perovskite Oxides for the Electrocatalytic Oxygen Evolution Reaction in Alkaline Electrolytes, *ACS Mater. Lett.*, 2024, **6**(12), 5227–5241.

28 M. Bilal, F. Ahmad, S. Zawar, U. Waqas, M. A. Khan, S. M. Ramay, *et al.*, Optimized Charge Dynamics of $Sr_2Fe_2O_5$/rGO Composite Electrodes: Redefining Supercapacitor Efficiency, *ECS J. Solid State Sci. Technol.*, 2024, **13**(2), 21001.

29 D. Tang, C. Shao, S. Jiang, C. Sun and S. Song, Graphitic C_2N_3: an allotrope of g-C_3N_4 containing active azide pentagons as metal-free photocatalyst for abundant H_2 bubble evolution, *ACS Nano*, 2021, **15**(4), 7208–7215.

30 F. Hadji, M. Omari, M. Mebarki, N. Gabouze and A. Layadi, Zinc doping effect on the structural and electrochemical properties of $LaCoO_3$ perovskite as a material for hybrid supercapacitor electrodes, *J. Alloys Compd.*, 2023, **942**, 169047.

31 P. M. Shafi, N. Joseph, A. Thirumurugan and A. C. Bose, Enhanced electrochemical performances of agglomeration-free $LaMnO_3$ perovskite nanoparticles and achieving high energy and power densities with symmetric supercapacitor design, *Chem. Eng. J.*, 2018, **338**, 147–156.

32 Y. Cao, B. Lin, Y. Sun, H. Yang and X. Zhang, Symmetric/asymmetric supercapacitor based on the perovskite-type lanthanum cobaltate nanofibers with Sr-SUBSTITUTION, *Electrochim. Acta*, 2015, **178**, 398–406.

33 S. Venkateshalu, G. Subashini, P. Bhardwaj, G. Jacob, R. Sellappan, V. Raghavan, *et al.*, Phosphorene, antimonene, silicene and siloxene based novel 2D electrode materials for supercapacitors-A brief review, *J. Energy Storage*, 2022, **48**, 104027.

34 S. Pappu, S. Anandan, T. N. Rao, S. K. Martha and S. V. Bulusu, High-performance hybrid supercapacitor with electrochemically exfoliated graphene oxide incorporated $NiCo_2O_4$ in aqueous and non-aqueous electrolytes, *J. Energy Storage*, 2022, **50**, 104598.

35 L. Li, Y. Jiang, C. Guo, K. Han, X. Cui, C. He, *et al.*, Mechanochemical production of graphene/amorphous carbon/Mn_3O_4 nanocomposites for asymmetric supercapacitor, *Appl. Surf. Sci.*, 2024, **653**, 159388.

36 M. B. Askari, P. Salarizadeh, A. Di Bartolomeo and F. Şen, Enhanced electrochemical performance of $MnNi_2O_4$/rGO nanocomposite as pseudocapacitor electrode material and methanol electro-oxidation catalyst, *Nanotechnology*, 2021, **32**(32), 325707.

37 F. Ahmad, M. A. Khan, U. Waqas, S. M. Ramay and S. Atiq, Elucidating an efficient super-capacitive response of a $Sr_2Ni_2O_5$/rGO composite as an electrode material in supercapacitors, *RSC Adv.*, 2023, **13**(36), 25316–25326.

38 A. Tariq, G. Ali, U. Waqas, K. J. Ahmad, S. M. Ramay, F. Afzal, *et al.*, Synergistic integration of rGO into cobalt oxide matrix for efficient electrochemical performance mediated by structural stability, *J. Energy Storage*, 2024, **80**, 110346, DOI: 10.1016/j.est.2023.110346.

39 A. Qayyum, M. O. ur Rehman, F. Ahmad, M. A. Khan, S. M. Ramay and S. Atiq, Performance optimization of Nd-

doped $LaNiO_3$ as an electrode material in supercapacitors, *Solid State Ionics*, 2023, **395**, 116227.

40 N. Bano, S. I. A. Shah, A. Sami, M. Ali, R. A. Alshgari, S. Mohammad, *et al.*, Development of binder–free Ni_3S_2/CoS_2 nano–composite as electrode material for energy storage application, *Ceram. Int.*, 2024, **50**(23), 49880–49888.

41 Z. Shi, G. Sun, R. Yuan, W. Chen, Z. Wang, L. Zhang, *et al.*, Scalable fabrication of $NiCo_2O_4$/reduced graphene oxide composites by ultrasonic spray as binder-free electrodes for supercapacitors with ultralong lifetime, *J. Mater. Sci. Technol.*, 2022, **99**, 260–269.

42 C. Bathula, I. Rabani, S. Ramesh, S. H. Lee, R. R. Palem, A. T. A. Ahmed, *et al.*, Highly efficient solid-state synthesis of Co_3O_4 on multiwalled carbon nanotubes for supercapacitors, *J. Alloys Compd.*, 2021, **887**, 161307.

43 A. K. Vats, A. Kumar, P. Rajput and A. Kumar, Engineered perovskite $LaCoO_3$/rGO nanocomposites for asymmetrical electrochemical supercapacitor application, *J. Mater. Sci.:Mater. Electron.*, 2022, 1–17.

44 I. Ajin, R. Balamurugan, S. S. Shalini, and A. C. Bose. Investigation on $SrCoO_3$ perovskites for supercapacitor applications, in *AIP Conference Proceedings*, AIP Publishing, 2024.

45 J. Xu, L. Wu, Y. Liu, J. Zhang, J. Liu, S. Shu, *et al.*, NiO-rGO composite for supercapacitor electrode, *Surf. Interfaces*, 2020, **18**, 100420.

46 S. I. El-Hout, S. G. Mohamed, A. Gaber, S. Y. Attia, A. Shawky and S. M. El-Sheikh, High electrochemical performance of rGO anchored CuS nanospheres for supercapacitor applications, *J. Energy Storage*, 2021, **34**, 102001.

47 G. Liu, L. Liu, G. Li, S. Wu, J. He, Y. Zhou, *et al.*, Temperature-Dependent Electrochemical Performance of Ta-Substituted $SrCoO_3$ Perovskite for Supercapacitors, *Chem.–Eur. J.*, 2024, **30**(14), e202303267.

48 L. Liu, G. Liu, S. Wu, J. He, Y. Zhou, M. Demir, *et al.*, Fe-substituted $SrCoO_3$ perovskites as electrode materials for wide temperature-tolerant supercapacitors, *Ceram. Int.*, 2024, **50**(1), 1970–1980.

49 S. M. Vidhi, A. K. Singh and O. P. Thakur, Synthesis of rGO/TiO_2 composite electrode material for enhanced electrochemical activity and its applications in supercapacitors, *Ionics*, 2024, 1–13.

50 J. Huang, K. Jiang, D. Tranca, C. Ke, L. Zhang, J. Li, *et al.*, Perovskite oxide and polyazulene–based heterostructure for high–performance supercapacitors, *J. Appl. Polym. Sci.*, 2021, **138**(41), 51198.

51 Z. M. Riyas and M. R. Prabhu, Microwave irradiation effect of La_2O_3–CeO_2 nanocomposites as a potential electrode material for asymmetric supercapacitor, *Ionics*, 2024, **30**(9), 5737–5754.

52 J. He, L. Cao, J. Cui, G. Fu, R. Jiang, X. Xu, *et al.*, Flexible energy storage devices to power the future, *Adv. Mater.*, 2024, **36**(4), 2306090.

53 J. Singh, A. Kumar and A. Kumar, Facile solvothermal synthesis of nano-assembled mesoporous rods of cobalt free–La_2NiFeO_6 for electrochemical behaviour, *Mater. Sci. Eng., B*, 2020, **261**, 114664.

54 D. Khalafallah, Y. Zhang, H. Dai, C. Liu and Q. Zhang, Manipulating the overall capacitance of hierarchical porous carbons *via* structure-and pore-tailoring approach, *Carbon*, 2024, **227**, 119250.

55 B. A. Khan, R. Hussain, A. Shah, A. Mahmood, M. Z. U. Shah, J. Ismail, *et al.*, $NiSe_2$ nanocrystals intercalated rGO sheets as a high-performance asymmetric supercapacitor electrode, *Ceram. Int.*, 2022, **48**(4), 5509–5517.

56 A. M. Idris, T. Liu, J. Hussain Shah, H. Han and C. Li, Sr_2CoTaO_6 double perovskite oxide as a novel visible-light-absorbing bifunctional photocatalyst for photocatalytic oxygen and hydrogen evolution reactions, *ACS Sustain. Chem. Eng.*, 2020, **8**(37), 14190–14197.

57 Z. Wei, Q. Wang, M. Qu and H. Zhang, Rational Design of Nanosheet Array-Like Layered-Double-Hydroxide-Derived $NiCo_2O_4$ In Situ Grown on Reduced-Graphene-Oxide-Coated Nickel Foam for High-Performance Solid-State Supercapacitors, *ACS Appl. Mater. Interfaces*, 2024, **16**(15), 18734–18744.

58 V. Lazarenko, R. Meija, Y. Rublova, A. Kons, V. Voikiva, J. Andzane, *et al.*, Bi_2Se_3@ SWCNT heterostructures with beyond theoretical capacity as perspective binder-free anodes for lithium-ion batteries, *J. Power Sources*, 2024, **593**, 233964.

59 P. R. Sørensen and T. Jacobsen, Conductivity, charge transfer and transport number—an ac-investigation of the polymer electrolyte LiSCN-poly (ethyleneoxide), *Electrochim. Acta*, 1982, **27**(12), 1671–1675.